

DIRECT NUMERICAL SIMULATION OF ROTATIONAL EFFECTS IN CYLINDRICAL GRAVITY CURRENTS

Jorge S. Salinas^a, Mariano I. Cantero^{a,b,c}, Thomas Bonometti^d and Enzo Dari^{a,b,c}

^a*Institute Balseiro, San Carlos de Bariloche, Río Negro, Argentina.*

^b*National Council for Scientific and Technological Research, San Carlos de Bariloche, Río Negro, Argentina.*

^c*Bariloche Atomic Center, National Commission of Atomic Energy, San Carlos de Bariloche, Río Negro, Argentina.*

^d*Institut de Mecanique des Fluides de Toulouse Groupe Ondes, Turbulence et Environnement*

Keywords: Density Currents, Rotational Effects, Turbulent Flows, Direct Numerical Simulation.

Abstract.

Gravity currents (also called density currents) are flows generated by horizontal pressure gradients, as a result of gravity over fluids with different density.

The study of these currents has a higher level of complication when the Coriolis force is present, as a result of earth's rotation, and the development of the flow is modified.

In this work we have addressed the rotational effects in gravity currents with cylindrical initial condition, by means of direct numerical simulations (DNS).

We have studied the oscillatory behavior of the front, and report on the frequency of these oscillations, finding that an increase in the velocity of rotation, produces an increase in these frequency.

We also found that at latest times, a steady-state lens shape characterizes all currents when a "Free slip" boundary condition is employed for the bottom wall. The maximum radius of this lens decrease as we increase the velocity of rotation. When we employed a "No slip" boundary condition at the bottom wall, the front acquires the same lens shape, but its radius continues to increase with time. This is a consequence of the imbalance of the Coriolis and buoyant forces, owing to the shear stress at the bottom wall.

Finally, we found turbulent structures not seen in non-rotating cylindrical gravity currents. A vertical vortex appears at the center of the current, and an array of quasi-streamwise Kelvin-Helmholtz vortices, owing to shear stress between the light and heavy fluid at the front.

1 INTRODUCTION

Gravity currents (also called density currents) are flows generated by horizontal pressure gradients, as a result of gravity over fluids with different density. These flows manifest as an horizontal current of light fluid above a heavy fluid, or as a current of heavy fluid below light fluid, and can be produced by a small density difference between the two fluids (García, 1992). In the turbulent regime, gravity currents are of a non-linear nature and exhibit a wide range of temporal and spatial scales.

Gravity currents are present in nature in many situations, like avalanches in the mountains, volcanic plumes, or sand storms in the desert. These natural phenomena play an important role in the transport of mass, momentum and energy. Works of Huppert and Simpson (1980), Fannelop and Waldman (1971), Hout (1972), studied the behavior of stratified currents by laboratory experiments and theoretical models.

When the current spread out in an horizontal plane, and has an unhindered motion in all directions, the front acquires a cylindrical shape (cylindrical currents). Three-dimensional highly resolved simulations of cylindrical density currents were studied by Cantero et al. (2007a), for different Reynolds numbers.

Earth's rotation brings another level of complication to the study of gravity currents, when the Coriolis force modifies drastically the development of the flow. Hallworth et al. (2001) reported on experimental and numerical investigations of axisymmetric gravity currents in a rotating system.

In this work we address the rotational effects in gravity currents with cylindrical initial condition by means of direct numerical simulations (DNS). We report on four three-dimensional direct numerical simulations with grid resolutions up to 118-million points, various boundary conditions ("Free slip" and "No slip"), and rotational velocities. We present results about macroscopical quantities, such as the maximum distance of propagation of the front in its first oscillation and in its steady-state lens shape and the frequency of the successive outward fronts. Also, we perform a detailed analysis of the characteristic turbulent structures present in rotating gravity current.

2 MATHEMATICAL AND NUMERICAL FORMULATION

The problem under consideration is depicted schematically in Fig. 1. It consists of a rectangular tank rotating at a constant angular velocity Ω_z along the vertical axis z . Co-rotating with the tank there is a heavy fluid of density ρ_1 , initially confined in a cylindrical region of radius r_0 and occupying the full height of the domain H (blue shaded area in fig. 1), separated from the lighter ambient co-rotating fluid of density ρ_0 . The heavy fluid is then released, and the flow spreads in the horizontal direction (x and y).

We consider flows in which the density difference is small enough that the Boussinesq approximation is valid. Under these circumstances, and in a system of reference attached to the tank, the dimensionless governing equations are

$$\frac{\partial \tilde{\mathbf{u}}}{\partial \tilde{t}} + \tilde{\mathbf{u}} \cdot \tilde{\nabla} \tilde{\mathbf{u}} = -\tilde{\nabla} \tilde{p} + \frac{1}{Re} \tilde{\nabla}^2 \tilde{\mathbf{u}} - \tilde{\rho} \hat{\mathbf{z}} - 2\tilde{C}(\tilde{v}\hat{\mathbf{x}} - \tilde{u}\hat{\mathbf{y}}), \quad (1)$$

$$\tilde{\nabla} \cdot \tilde{\mathbf{u}} = 0, \quad (2)$$

$$\frac{\partial \tilde{\rho}}{\partial \tilde{t}} + \tilde{\mathbf{u}} \cdot \tilde{\nabla} \tilde{\rho} = \frac{1}{Re Sc} \tilde{\nabla}^2 \tilde{\rho}. \quad (3)$$

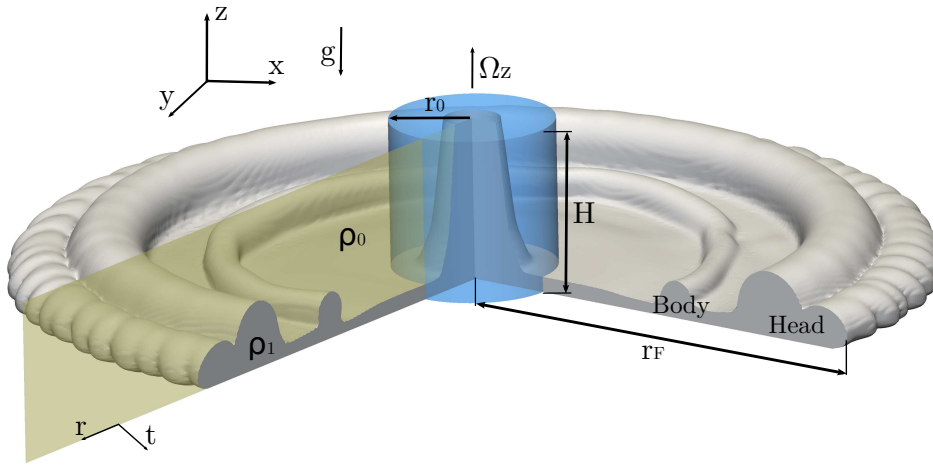


Figure 1: Schematic of the configuration for the cylindrical system.

Here, $\tilde{\mathbf{u}} = \{\tilde{u}, \tilde{v}, \tilde{w}\}$ is the dimensionless velocity, \tilde{p} the dimensionless pressure, and the dimensionless parameters are the Reynolds, Schmidt, and Coriolis numbers defined as

$$Re = \frac{UH}{\nu}, \quad Sc = \frac{\nu}{\kappa} \quad \text{and} \quad \tilde{C} = \frac{\Omega_z H}{U}, \quad (4)$$

where ν is the kinematic viscosity and κ the molecular diffusivity.

In equations (1)-(3), we have employed the length scale H , the velocity scale $U = \sqrt{RgH}$ with $R = (\rho_1 - \rho_0)/\rho_0$, and the time scale $T = H/U$. The dimensionless density is given by

$$\tilde{\rho} = \frac{\rho - \rho_0}{\rho_1 - \rho_0}. \quad (5)$$

The governing equations (1)-(3) are solved in a dimensionless rectangular box of size $\tilde{L}_x \times \tilde{L}_y \times \tilde{H}$, with periodic boundary conditions along the horizontal directions \tilde{x} and \tilde{y} for all the variables. Because the current spreads in the radial direction along the horizontal (\tilde{x} - \tilde{y}) plane, we set $\tilde{L}_x = \tilde{L}_y$.

We have employed a fully de-aliased pseudo-spectral code (Canuto et al., 1988), in which Fourier expansions are employed along the horizontal directions \tilde{x} and \tilde{y} . In the vertical direction \tilde{z} , a Chebyshev expansion is used with Gauss-Lobatto quadrature points (Canuto et al., 1988). The flow field is time advanced using a Crank-Nicolson scheme for the diffusion terms. The advection terms are handled with the Arakawa method (Durrant, 1999) and advanced with a third-order Runge-Kutta scheme. The buoyancy term is also advanced with a third-order Runge-Kutta scheme. At the top and bottom walls, a zero-gradient condition is enforced for the density field $\tilde{\rho}$. We have employed different boundary conditions for velocity at the bottom and top walls (detailed in Table 1).

3 RESULTS AND DISCUSSION

In this work we present four simulations of cylindrical gravity currents with the geometrical configuration depicted in figure 1. A detailed description of the cases studied is presented in Table 1. Case (1) to (3) only differ in the Coriolis parameter, and case (4) has a different boundary condition at the bottom wall (“No Slip”). All simulations have a “Free Slip” boundary condition at the top wall.

case	\tilde{C}	Re	$\tilde{L}_x \times \tilde{L}_y \times \tilde{H}$	$N_x \times N_y \times N_z$	$B.C.$	\bar{r}_{max}	\bar{r}_{lens}	$\bar{\omega}_p$
1	0.1	4000	$18 \times 18 \times 1$	$960 \times 960 \times 128$	<i>FreeSlip</i>	7.2	6.3	0.2
2	0.15	4000	$15 \times 15 \times 1$	$768 \times 768 \times 128$	<i>FreeSlip</i>	5.7	5.3	0.3
3	0.25	4000	$15 \times 15 \times 1$	$768 \times 768 \times 128$	<i>FreeSlip</i>	4.2	4.1	0.5
4	0.15	4000	$15 \times 15 \times 1$	$768 \times 768 \times 128$	<i>NoSlip</i>	4.5	—	0.37

Table 1: Numerical simulations studied in this work. Also shown are the boundary conditions employed for the velocity at the bottom wall ($B.C.$), the values of the maximum distance of propagation of the front (\bar{r}_{max}), the radius of the steady state lens shape (\bar{r}_{lens}), and the frequency of the subsequent fronts for the rotating currents ($\bar{\omega}_p$).

3.1 Effects of rotation in cylindrical gravity currents: Coriolis parameter

The velocity of rotation of the system, and hence the Coriolis parameter, has a great impact in the development of the flow. In this section we discuss the flow dynamics and the quasi-steady state lens shape acquired by the current.

3.1.1 Maximum distance of propagation of the front: The steady state lens shape

For the computation of the maximum distance of propagation of the front we define a local equivalent height \tilde{h} . Shin et al. (2004) and Marino et al. (2005) define a local equivalent height in an unambiguous way as

$$\tilde{h}(\tilde{r}, \tilde{\theta}, \tilde{t}) = \int_0^1 \tilde{\rho} d\tilde{z}. \quad (6)$$

At locations where the entire layer is occupied by the heavy fluid, the equivalent height is unity, whereas at locations where the light fluid fills the entire layer, the equivalent height \tilde{h} is zero. The local current height can then be averaged over the azimuthal direction. We define the mean equivalent height as

$$\bar{h}(\tilde{r}, \tilde{t}) = \frac{1}{2\pi} \int_0^{2\pi} \tilde{h}(\tilde{r}, \tilde{\theta}, \tilde{t}) d\tilde{\theta}. \quad (7)$$

The mean front location \bar{r}_F can now be defined as the radial position where the mean equivalent height \bar{h} , becomes smaller than a small threshold δ . Precise definition can be found in Cantero et al. (2007b). For the computation of the maximum distance of propagation of the front, in its first oscillation, the threshold $\bar{h} = 0.01$ is used.

Because we will study cylindrical gravity currents, the mean flow will be computed as

$$\bar{f}(\tilde{r}, \tilde{z}, \tilde{t}) = \frac{1}{2\pi} \int_0^{2\pi} \tilde{f}(\tilde{r}, \tilde{\theta}, \tilde{z}, \tilde{t}) d\tilde{\theta}, \quad (8)$$

where \tilde{f} is the density field $\tilde{\rho}$, or the velocity field $\tilde{\mathbf{u}}$.

Figure 2 shows the front location as a function of time for different thresholds of \bar{h} , for cases (1) to (3). In all cases, the front starts to accelerate, until the velocity of the front becomes zero and the current start to move inward. This first inflection happens for $\bar{h} = 0.01$ at $\tilde{t} \approx 20$, $\tilde{t} \approx 15$, $\tilde{t} \approx 12$, for cases (1) to (3), respectively. The first oscillation of the front happens before as the Coriolis parameter increases. The front oscillations repeat several times with attenuated amplitude until the flow reaches eventually its steady state. At the first oscillation, the maximum distances of propagation of the fronts are $\bar{r}_{max} = 7.2$, $\bar{r}_{max} = 5.7$ and $\bar{r}_{max} = 4.2$, for cases

(1) to (3), respectively. As we could expect, less propagation in the positive radial direction occur with increasing velocity of rotation of the system. At later times, when the flow is in its steady state lens shape, the mean distance of propagation of the front \bar{r}_{lens} (the mean radius of the lens) is also influenced by the Coriolis parameter, being this values $\bar{r}_{lens} = 6.3$, $\bar{r}_{lens} = 5.3$ and $\bar{r}_{lens} = 4.1$, for cases (1) to (3) respectively. The values of \bar{r}_{max} and \bar{r}_{lens} are also shown in Table 1.

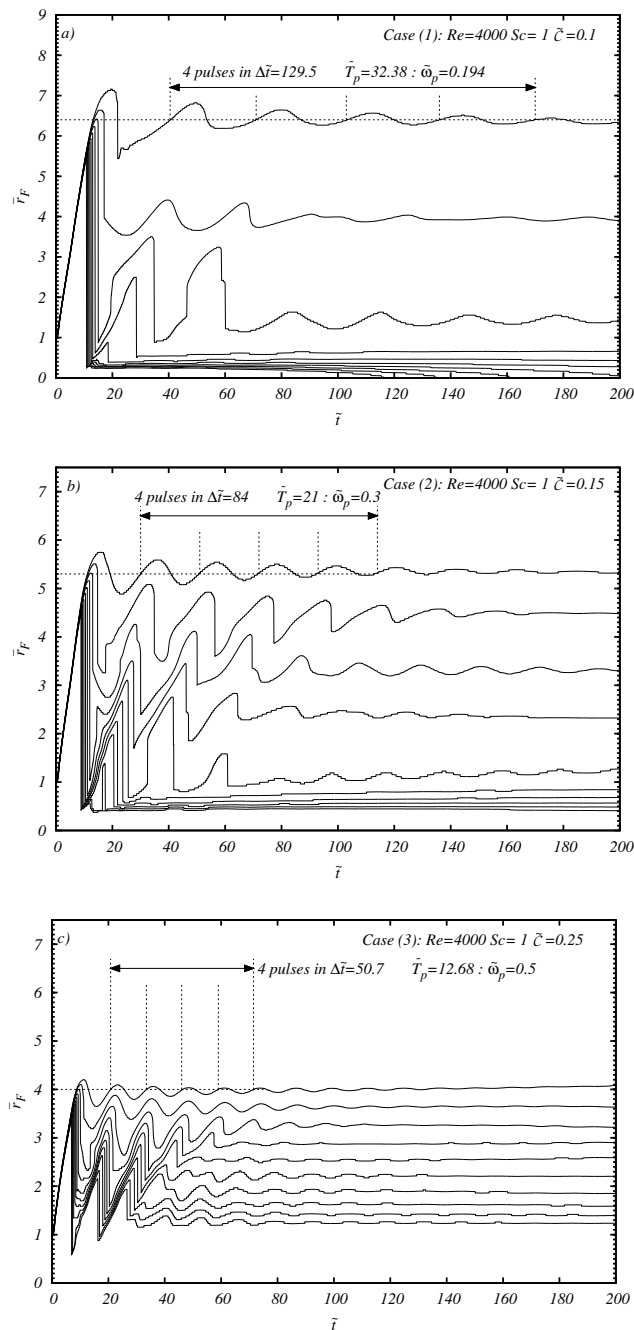


Figure 2: Front location \bar{r}_F as a function of time \tilde{t} for different thresholds of \bar{h} , from $\bar{h} = 0.01$ to $\bar{h} = 0.1$, for a)Case (1), b)Case (2), c)Case (3). All three simulations have “Free Slip - Free Slip” boundary conditions at the bottom and top walls, respectively.

3.1.2 Frequency of oscillation of the front

As it was described in the previous section, the front's position of the cylindrical gravity currents has an oscillatory behavior until the flow reaches the steady state lens shape.

The mean pulse period \bar{T}_p for each simulation is defined as the averaged time interval on which the successive outward fronts, tracked by $\bar{h} = 0.01$, reach a fixed radial distance \bar{r} . The pulse frequency $\bar{\omega}_p$ is defined as

$$\bar{\omega}_p = \frac{2\pi}{\bar{T}_p}. \quad (9)$$

Values of $\bar{\omega}_p$ for all simulations are shown in Table 1 and Fig. 2.

Comparing the mean pulse frequency of the successive outward fronts $\bar{\omega}_p$, we find a linear dependence with the Coriolis parameter:

$$\bar{\omega}_p = 2\tilde{\mathcal{C}}. \quad (10)$$

Similar results are reported by Hallworth et al. (2001) with laboratory experiments of axisymmetric gravity currents.

3.1.3 Mean velocity profiles in the tangential and radial directions

The oscillations present in the flow are better understood by the analysis of mean velocity profiles of the current. We will explain the development of the flow for case (3), with the highest Coriolis parameter of $\tilde{\mathcal{C}} = 0.25$. After this, a comparison with cases (1) and (2) will be made. We use the cylindrical axis configuration shown in Fig. 1.

The mean radial velocity profiles (\bar{u}_r) as a function of \tilde{z} for case (3) are presented in Fig. 3 for radial positions $\bar{r} = 1$ and $\bar{r} = 3$. Fig. 4 shows the mean tangential velocity profiles (\bar{u}_t) as a function of the radial position \bar{r} for $\tilde{z} = 0.025$ and $\tilde{z} = 0.975$, also for case (3).

When the heavy fluid is released and starts to move in the positive radial direction as a result of the buoyancy force, a Coriolis force in the negative tangential direction is produced, and hence, a flow in this direction. This effect can be seen in Fig. 3a for $\tilde{t} = 2.5$, where a velocity in the positive radial direction $\bar{u}_r \approx 0.66$ produces a Coriolis force in the negative tangential direction and a velocity $\bar{u}_t \approx 0.4$ in the negative tangential direction at the front (see Fig. 4 at $\tilde{z} = 0.025$ and $\bar{r} \approx 2$).

At $\tilde{t} = 5$, the front is still moving in the positive radial direction, but at $\bar{r} \approx 1$ (see Fig. 3a for $\tilde{t} = 5$) the buoyancy force can not longer balance the Coriolis force in the negative radial direction produced by the velocity \bar{u}_t in the negative tangential direction, and a secondary current starts to move in the negative radial direction. This can be seen in Fig. 3 for $\tilde{t} = 5$ and $\tilde{z} \approx 0$, where $\bar{u}_r \approx -0.22$.

At the front of the current, the flow in the negative tangential direction at $\bar{r} \approx 3$ (see Fig. 4 for $\tilde{z} = 0.025$), produces a Coriolis force in the negative radial direction, but this force is not as strong as the buoyancy force in the front, and hence, the front still moves in the positive radial direction.

At $\tilde{t} = 10$, the body of the current is moving in the negative radial direction, and when it arrives to the center of the domain ($\bar{r} = 0$), the current is reflected in the opposite direction. This can be seen in Fig. 3a at $\tilde{t} = 10$, where a secondary wave is moving in the positive radial direction at $\tilde{z} \approx 0.28$, over the main current moving in the negative radial direction at $\tilde{z} \approx 0$. As this secondary wave starts to move outward, the body of the current is still moving inward (see

Fig. 3b at $\tilde{t} = 10$ for $\bar{r} = 3$), and the head is moving outward. At $\tilde{t} \approx 12$, the Coriolis force in the negative radial direction (produced by the flow in the negative tangential direction) balance and surpass the buoyancy force in the opposite direction, making the head of the current move in the negative radial direction (see Fig. 2c) for $\tilde{t} \approx 12$).

At $\tilde{t} = 20$, the secondary wave that we saw at $\tilde{t} = 10$, catches up with the head of the current and the second oscillation of the front occurs (see 2c for $\tilde{t} \approx 20$). This flow in the positive radial direction produces again a Coriolis force in the negative tangential direction, and the process described before repeats itself several times after.

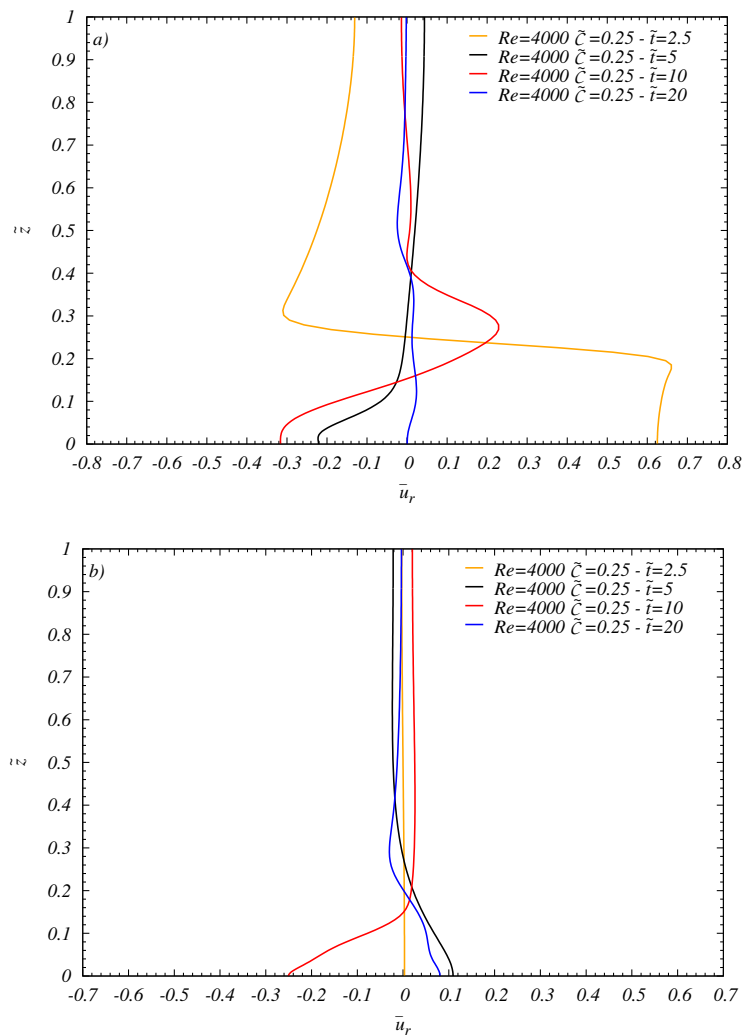


Figure 3: Mean radial velocity \bar{u}_r as a function of height \tilde{z} for a) $\bar{r} = 1$, b) $\bar{r} = 3$, for case (3).

At about $\tilde{t} = 100$, the amplitude of the oscillations in the front position drops significantly, and the current acquires the steady state lens shape. As we can see in Fig. 5 for $\tilde{t} \geq 100$, the mean radial velocity \bar{u}_r is practically zero.

Figures 6 and 7 show the mean radial velocity profiles for $\bar{r} = 1$, for cases (1) and (2), respectively. Comparing figures 3, 6 and 7 for $\bar{r} = 1$ and $\tilde{t} = 2.5$, we see that the mean radial velocity of the heavy fluid is lower with increasing Coriolis parameter ($\bar{u}_r \approx 0.74$, $\bar{u}_r \approx 0.70$, $\bar{u}_r \approx 0.62$, for $\tilde{C} = 0.1$, $\tilde{C} = 0.15$ and $\tilde{C} = 0.25$, respectively). This is because an increase in the velocity of rotation of the system, produces a stronger Coriolis force in the negative tangential

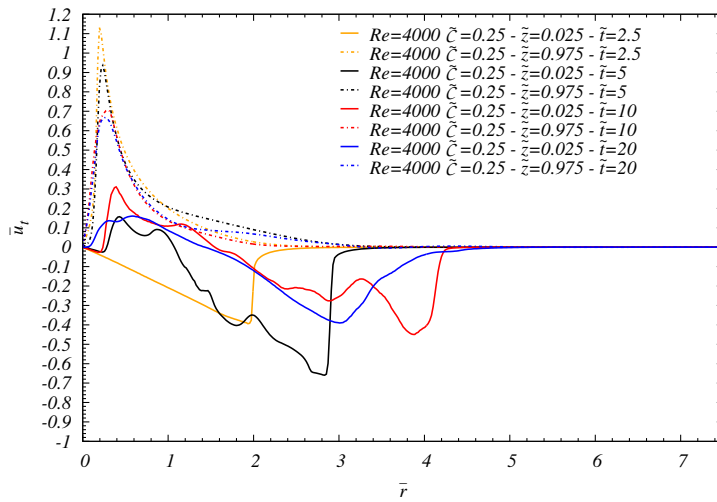


Figure 4: Mean tangential velocity \bar{u}_t as a function of \bar{r} , for $\tilde{z} = 0.025$ and $\tilde{z} = 0.975$, for case (3).

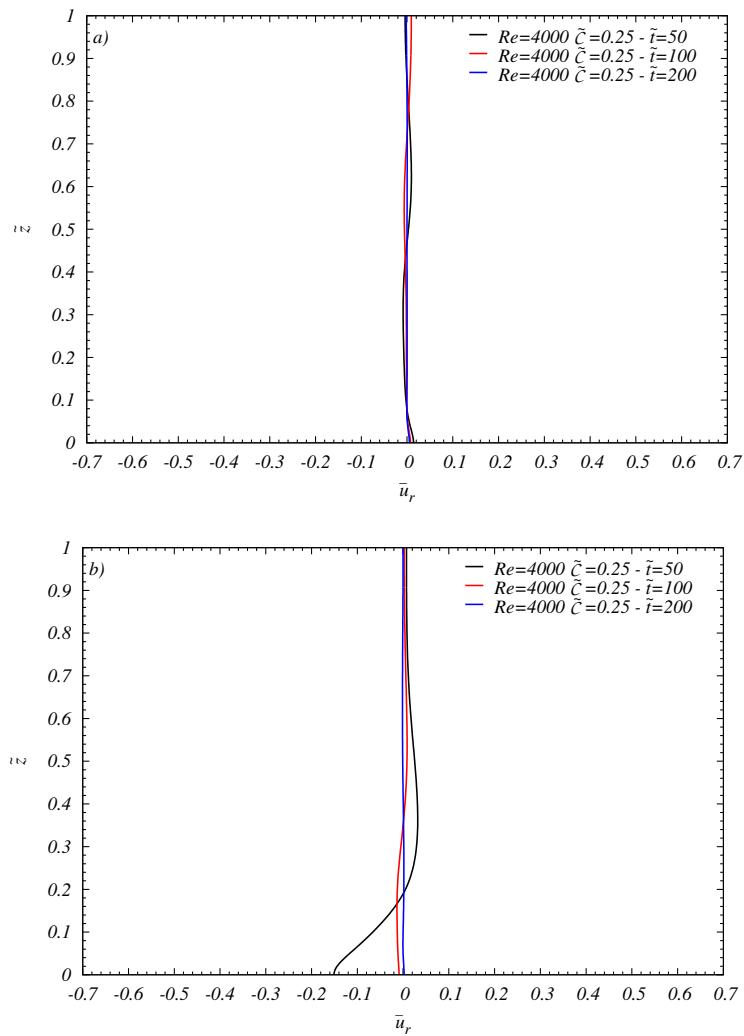


Figure 5: Mean radial velocity \bar{u}_r as a function of height \tilde{z} for a) $\bar{r} = 1$, b) $\bar{r} = 3$, for case (3) at latest times.

direction, that generates a higher negative tangential flow. This higher flow produce a stronger Coriolis force in the negative radial direction that pushes the flow inward.

At $\tilde{t} = 5$, a secondary flow in the negative radial direction produced by the Coriolis force is not yet present in cases (1) and (2), but it is in case (3). This can be seen in Fig. 3, 6 and 7 for $\bar{r} = 1$ and $\tilde{t} = 5$, where for case (3) the radial velocity at the bottom wall is $\bar{u}_r \approx -0.22$, and for cases (2) and (1) is $\bar{u}_r \approx 0.08$ and $\bar{u}_r \approx 0.2$, respectively. After this, at $\tilde{t} = 10$, the secondary flow is already reflected at the center of the domain in case (3), but is still moving in the negative radial direction in cases (1) and (2).

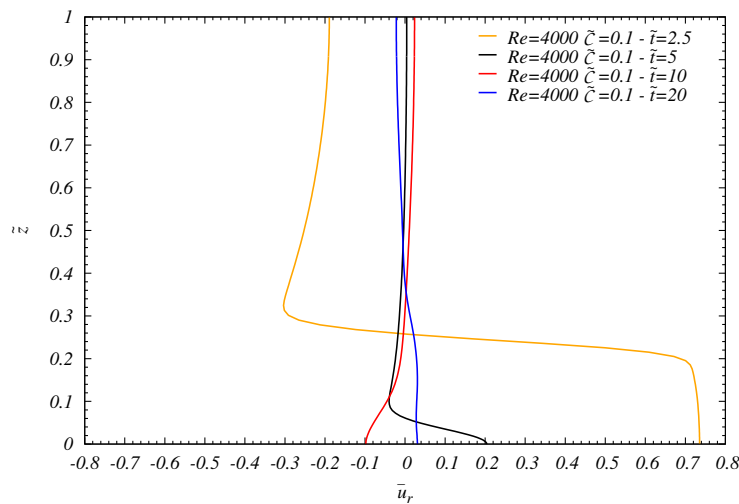


Figure 6: Mean radial velocity \bar{u}_r , at $\bar{r} = 1$, as a function of height \tilde{z} for case (1).

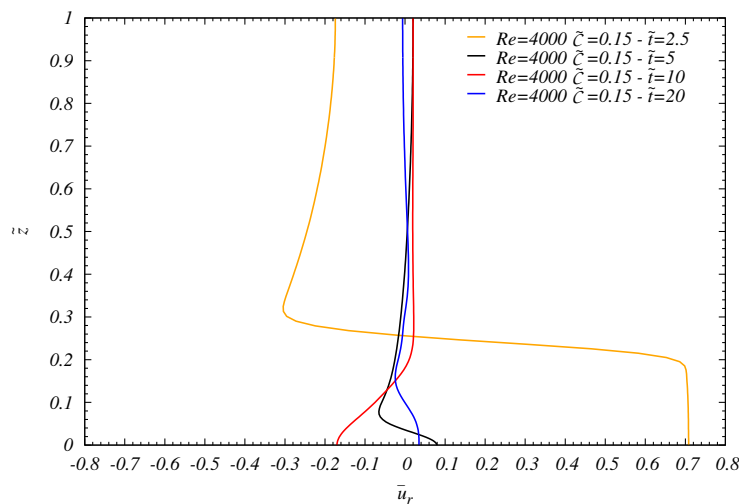


Figure 7: Mean radial velocity \bar{u}_r , at $\bar{r} = 1$, as a function of height \tilde{z} for case (2).

3.2 Effects of boundary conditions in rotating gravity currents

The boundary condition at the bottom wall influences drastically quantities such as \bar{T}_{max} , \bar{T}_{lens} and $\bar{\omega}_p$.

In this section we compare cases (2) and (4), where the only difference between these two simulations is the boundary condition at the bottom wall: Case (2) with a “Free Slip” boundary condition, and case (4) with “No Slip”.

Fig. 8 shows the front location as a function of time, for different thresholds of \bar{h} , for case (4). Here we can see that the flow in the radial direction for case (4) is restricted by the shear stress at the bottom of the domain. As a result, the maximum radius of the first outward front \bar{r}_{max} is smaller than in case (2) ($\bar{r}_{max} = 5.7$ and $\bar{r}_{max} = 4.5$, for cases (2) and (4), respectively). This difference can also be seen comparing Figs. 7 and 9, where mean radial velocity profiles (\bar{u}_r) as a function of \tilde{z} are presented for radial position $\tilde{r} = 1$, for cases (2) and (4), respectively. At $\tilde{t} = 2.5$ and $\tilde{r} = 1$, the positive radial velocity at $\tilde{z} < 0.04$ for case (4) is lower than for case (2), producing a weaker Coriolis force in the negative tangential direction, and hence, lower negative tangential velocities of the flow. Lower radial velocities are also seen for times $\tilde{t} = 5$, $\tilde{t} = 10$ and $\tilde{t} = 20$.

Another distinctive difference is that the maximum radius of the successive outward fronts for case (4) are not smaller than of the previous oscillations (see fig. 8), behavior seen in case (2) (see fig. 2b). This can be explained analyzing figures 10 and 11, where we present mean tangential velocity profiles (\bar{u}_t) as a function of the radial position \bar{r} for $\tilde{z} = 0.025$ and $\tilde{z} = 0.975$, for cases (2) and (4), respectively. As we explained with figures 7 and 9, lower radial velocities seen in the flow for case (4), produces a weaker Coriolis force in the negative tangential direction, and lower tangential velocities. This can be seen in figures 10 and 11, where lower negative tangential velocities for $\tilde{z} = 0.025$ are reached in the heavy fluid, for case (4). This lower tangential velocity produces a weaker Coriolis force in the negative radial direction, allowing the maximum radius reached at each oscillation to be greater than the maximum radius at the previous oscillation. At later times ($\tilde{t} > 80$), the Coriolis force in the negative radial direction can not balance the boundary force, and as a result, a quasi-steady state lens shape is not reached.

Also, an increase in the frequency of the successive outward fronts $\bar{\omega}_p$ is observed in case (4) (see fig. 2b and 8).

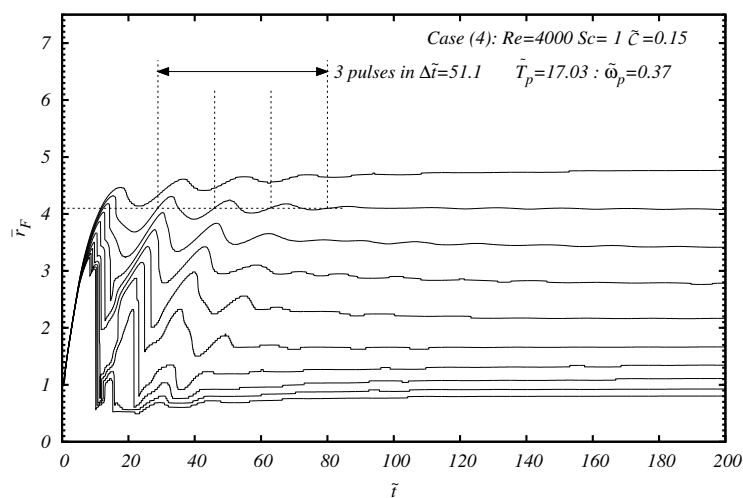


Figure 8: Front location \bar{r}_F as a function of time \tilde{t} for different thresholds of \bar{h} (from $\bar{h} = 0.01$ to $\bar{h} = 0.1$), for case (4).

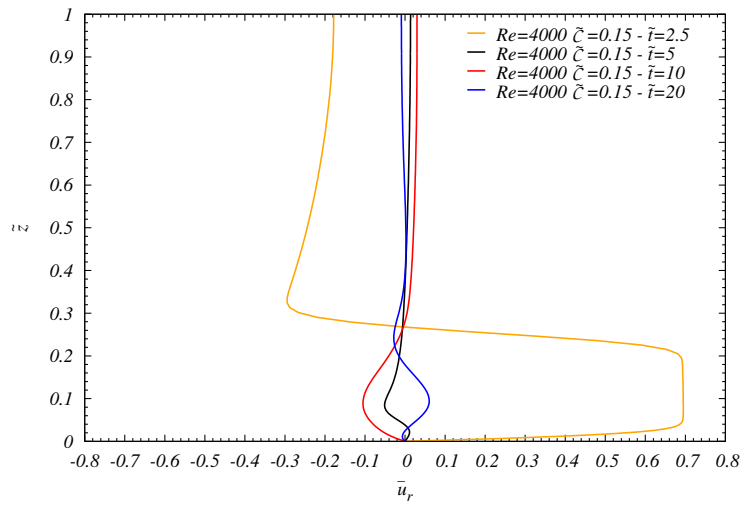


Figure 9: Mean radial velocity \bar{u}_r , at $\bar{r} = 1$, as a function of height \tilde{z} for case (4).

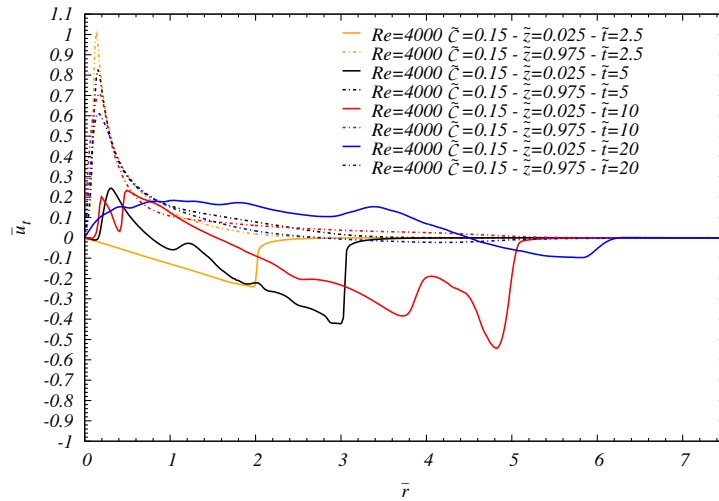


Figure 10: Mean tangential velocity \bar{u}_t as a function of \bar{r} , for $\tilde{z} = 0.025$ and $\tilde{z} = 0.975$, for case (2).

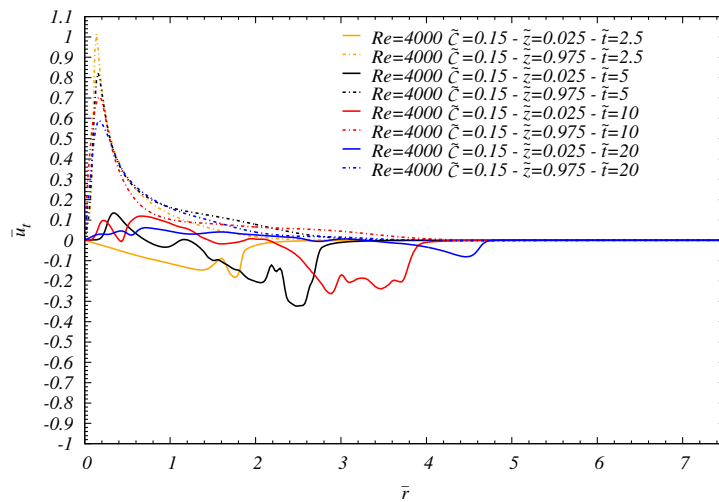


Figure 11: Mean tangential velocity \bar{u}_t as a function of \bar{r} , for $\tilde{z} = 0.025$ and $\tilde{z} = 0.975$, for case (4).

3.3 Influence of rotation in three-dimensional flow structures

The presence of the Coriolis force generates distinctive turbulent structures, not present in a flow without rotation. Fig. 12 shows these characteristic structures and its effect on the interface between the light and heavy fluid for case (2). Fig. 12a shows the three-dimensional structure of the interface, where an isosurface of density $\tilde{\rho} = 0.05$ is shown for time $\tilde{t} = 7.5$. Also in this figure are depicted isocontours of density for $\tilde{y} = 0$ (gray contours). Fig. 12b shows the isosurface of “swirling strength” $\tilde{\lambda}_{ci} = 4$ for the same time. The “swirling strength” can be defined as the absolute value of the imaginary portion of the complex eigenvalues of the local velocity gradient tensor $\nabla\tilde{\mathbf{u}}$, and gives a means to determine the compactness of the vortical structures of the flow (see Zhou and Kendall (2005) and Chakraborty and Adrian (2005)).

In Fig. 12, although the body of the current has azimuthal symmetry, the interface at the head of the current is highly influenced by the quasi-streamwise Kelvin-Helmholtz vortices *KH2* surrounding the main Kelvin-Helmholtz vortex core *KH1*.

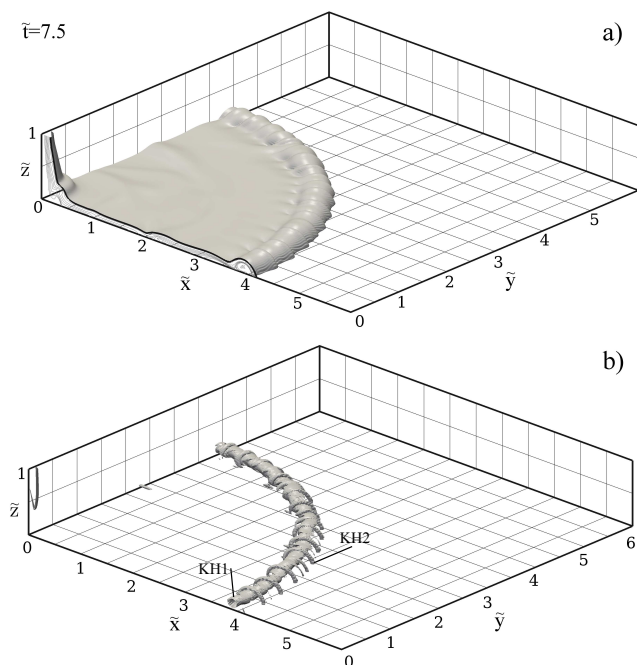


Figure 12: a) Three-dimensional structure of the interface visualized by an isosurface of density $\tilde{\rho} = 0.05$ at $\tilde{t} = 7.5$, for case (2). Also in this figure are depicted isocontours of density for $\tilde{y} = 0$ (gray contours); b) Isosurface of swirling strength $\tilde{\lambda}_{ci} = 4$ at $\tilde{t} = 7.5$, for case (2).

We address the influence of rotation by analyzing case (4), where a “No-Slip” boundary condition at the bottom wall is imposed, and produces more complex and developed turbulent structures. Fig. 13 shows the three-dimensional structure of the interface between the light and heavy fluid, where an isosurface of density $\tilde{\rho} = 0.05$ is presented for different times. This figure also shows isocontours of density for $\tilde{y} = 0$ (gray contours). Fig. 14 shows isosurfaces of swirling strength $\tilde{\lambda}_{ci}$ for the same time instances as in Fig. 13.

In Fig. 14a (for time $\tilde{t} = 5$) it can be seen the Kelvin-Helmholtz vortices *KH1* and *KH1'*, rotating counter-clockwise, formed at the first stages of development of the flow, and a secondary Kelvin-Helmholtz vortex core *KH2* between the first. This secondary vortex core *KH2* and vortex *KH1'* stops its radial motion at about $\tilde{t} \approx 7.5$ as a result of the Coriolis force in the negative radial direction.

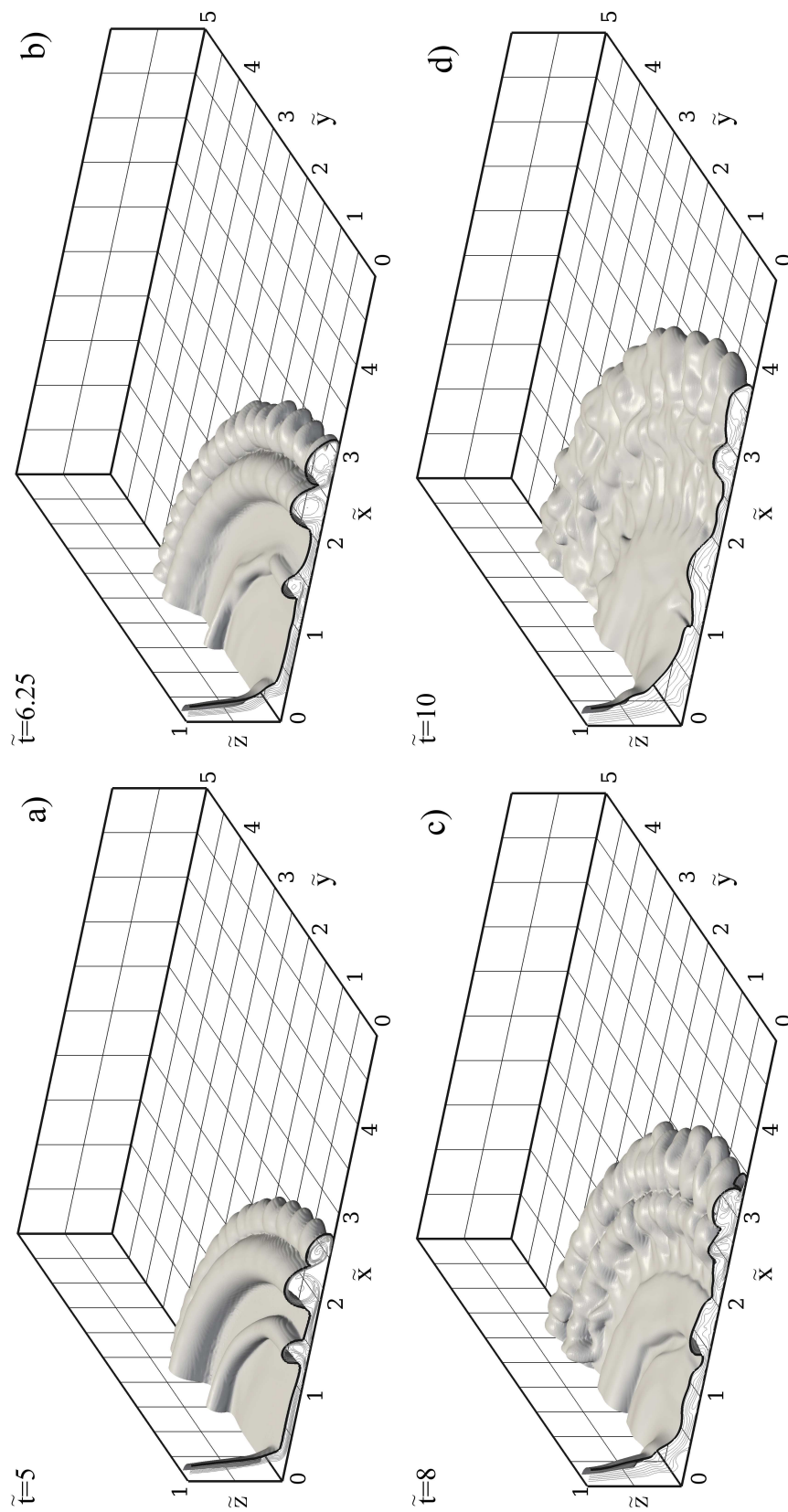


Figure 13: Three-dimensional structure of the interface visualized by isosurfaces of density $\tilde{\rho} = 0.05$ for case (4). Also in this figure are depicted isocontours of density for $\tilde{y} = 0$ (gray contours). a) $\tilde{t} = 5$; b) $\tilde{t} = 6.25$; c) $\tilde{t} = 8$; d) $\tilde{t} = 10$.

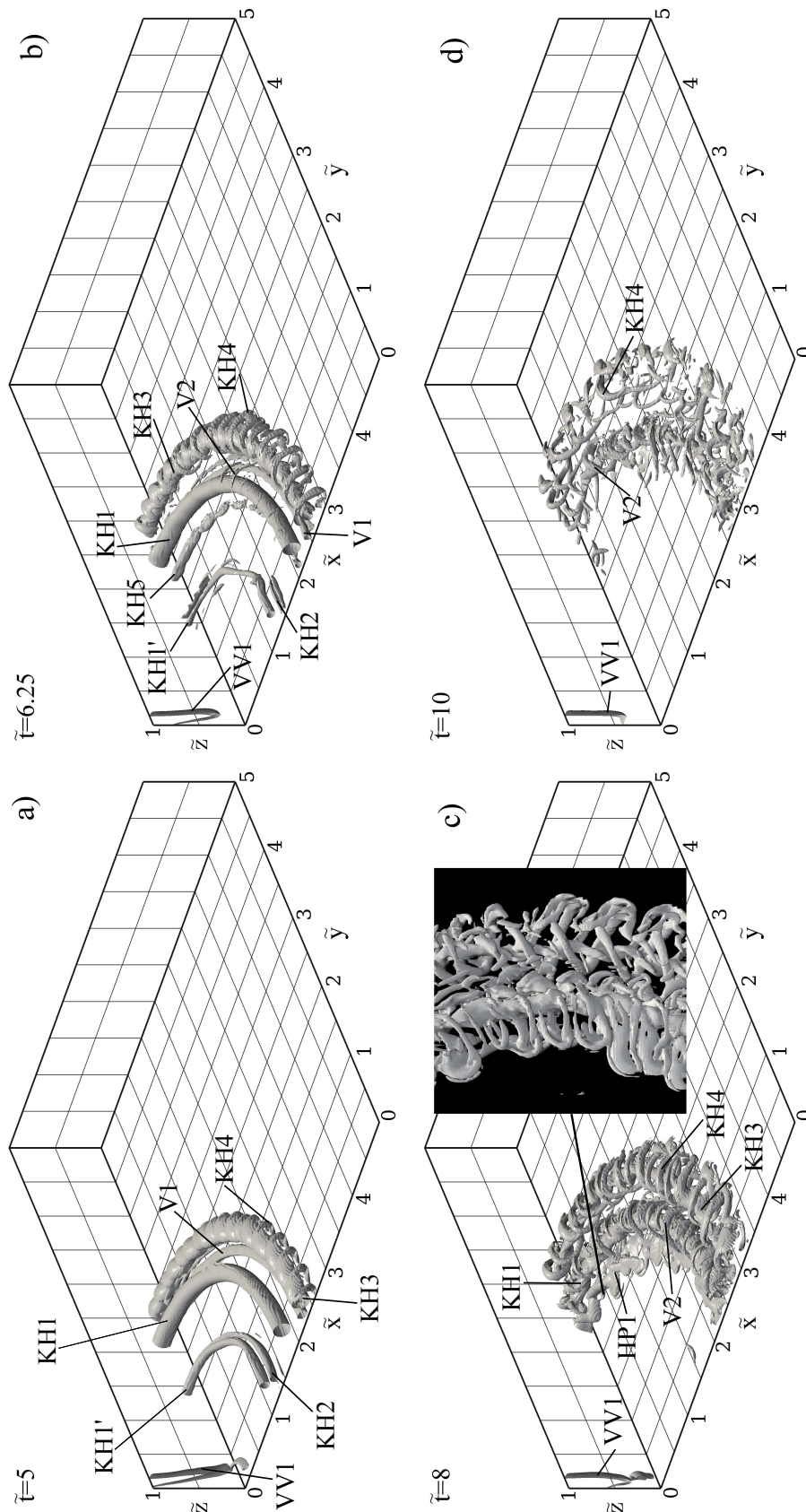


Figure 14: Isosurface of swirling strength $\tilde{\lambda}_{ci} = 2.5$ for case (4). a) $\tilde{t} = 5$; b) $\tilde{t} = 6.25$; c) $\tilde{t} = 8$; d) $\tilde{t} = 10$.

Also in Fig. 14a, a clockwise-rotating vortex $V1$, appears in front of vortex $KH1$ at the bottom, as a result of shear stress, and a Kelvin-Helmholtz vortex $KH3$ at the nose. As a consequence of rotation, a vertical vortex core $VV1$ is present at the center of the domain (until $\tilde{t} \approx 25$), and an array of quasi-streamwise Kelvin-Helmholtz vortices $KH4$ form surrounding vortex core $KH3$.

All Kelvin-Helmholtz vortices are produced by shear stress. Kelvin-Helmholtz vortex cores $KH1$, $KH1'$, $KH2$ and $KH3$, are the result of radial shear stress between the light and heavy fluid, and vortices $KH4$ are the result of tangential shear stress between the two fluids.

In Fig. 14b, for $\tilde{t} = 6.25$, a new vortex core $KH5$ forms behind vortex $KH1$, when a secondary flow starts to move inward, as a result of the Coriolis force in the negative radial direction. Also, it can be seen a loss of the strength of vortices $KH1'$ and $KH2$. Between the lobes at the front (see fig. 14b), the quasi-streamwise vortices $KH4$ are now connected to streamwise vortices at the bottom, that end up rising to the top and surrounding the Kelvin-Helmholtz vortex $KH1$. This array of vortices is $V2$ in Fig. 14b. At time $\tilde{t} = 8$ (Fig. 14c), vortices $V2$ grow in strength, while vortex core $KH1'$ is now too weak to be seen in an isosurface of $\lambda_{ci} = 2.5$

Kelvin-Helmholtz vortices $KH1$ and $KH3$ twist and stretch, while the array of quasi-streamwise vortices $KH4$ at the front stretch in the radial direction and move in the negative tangential direction. A connection between all the $KH4$ vortices can be seen, forming a toroidal spiral around vortex $KH3$. A bottom view of the front (inset in fig. 14c), shows a set of hairpin vortices $HP1$ behind vortex $KH1$, weakly connected to vortices $V2$.

At time $\tilde{t} = 10$ (fig. 14d), Kelvin-Helmholtz vortex cores $KH1$ and $KH3$ split in smaller turbulent structures, interacting with the quasi-streamwise vortices $KH4$ and $V2$. The latest, stretch in the tangential direction as a result of the Coriolis force, and continue to lose strength through time.

4 CONCLUSIONS

We have addressed the effect of rotation in gravity currents for a cylindrical configuration by direct numerical simulation. An oscillatory behavior of the flow is observed. This is documented by tracking the mean front position \bar{r}_F . At later times, a steady-state lens shape characterizes all currents when a *Free slip* boundary condition is employed for the bottom wall. When a *No slip* boundary condition is employed for the bottom wall, the lens shape is reached but its radius continues to increase with time owing to the imbalance of the Coriolis and buoyant forces.

With increasing Coriolis parameter \tilde{C} , a more restricted development of the flow is observed, being the maximum radius at the first oscillation of the front $\bar{r}_{max} = 7.2$, $\bar{r}_{max} = 5.7$ and $\bar{r}_{max} = 4.2$, for $\tilde{C} = 0.1$, $\tilde{C} = 0.15$ and $\tilde{C} = 0.25$, respectively. Also, in the cases where the flow reaches steady state, the mean distance of propagation of the front \bar{r}_{lens} (the mean radius of the lens) is also influenced by the Coriolis parameter, being these values $\bar{r}_{lens} = 6.3$, $\bar{r}_{lens} = 5.3$ and $\bar{r}_{lens} = 4.1$, for $\tilde{C} = 0.1$, $\tilde{C} = 0.15$ and $\tilde{C} = 0.25$, respectively.

We explained these behaviors by the analysis of mean radial and tangential velocity profiles. When the front moves in the positive radial direction, a Coriolis force appears in the negative tangential direction. This Coriolis force produces a flow in the same direction, and this tangential flow in turn produces a Coriolis force in the negative radial direction. When the buoyancy force can not balance this Coriolis force, the front starts to move inward.

After the first arrest of the front, several oscillations in the front position can be seen. A linear

relation between the Coriolis parameter and the frequency of these oscillations was found:

$$\bar{\omega}_p = 2\tilde{C}.$$

We also found that boundary conditions at the bottom wall influence the front position. When "No-slip" boundary condition is enforced, the shear stress at the bottom wall restricts the flow in the radial direction, producing a lower maximum radius at the first outward front ($\bar{r}_{max} = 4.5$ and $\bar{r}_{max} = 5.7$, for "No-Slip" and "Free-Slip", respectively). This lower radial velocity, generates a weaker Coriolis force in the negative tangential direction, and combined with the shear stress at the bottom, produces lower tangential velocities. This lower tangential velocity produces a weaker Coriolis force in the negative radial direction that can not balance the buoyancy force at later times, and as a result, the steady state lens shape is not reached.

Finally, we have identified the distinctive turbulent structures present in rotating cylindrical gravity currents. A vertical vortex core *VV1* appears at the center of the domain, and an array of quasi-streamwise Kelvin-Helmholtz vortices *KH4*, interconnected and forming a toroidal spiral around Kelvin-Helmholtz vortex core *KH3*. All turbulent structures are stretched and bended by the Coriolis forces in the radial and tangential directions, and even we can see a Kelvin-Helmholtz vortex *KH5* at a secondary inward front.

REFERENCES

- Cantero M., Balachandar S., and García M. Highly resolved simulations of cylindrical density currents. *Journal of Fluid Mechanics*, 590:437–469, 2007a.
- Cantero M., Lee J.R., Balachandar S., and García M. On the front velocity of gravity currents. *Journal of Fluid Mechanics*, 586:1–39, 2007b.
- Canuto C., Hussaini M., Quarteroni A., and Zang T. *Spectral Methods in Fluid Dynamics*. Springer-Verlag, New York, 1988. 557 pages.
- Chakraborty P. S.B. and Adrian R. On the relationships between local vortex identification schemes. *J. Fluid Mech.*, 535:189–214, 2005.
- Durrant D. *Numerical Methods for Wave Equations in Geophysical Fluid Dynamics*. Springer, 1999.
- Fannelop T. and Waldman G. The dynamics of oil slicks – or 'creeping crude'. *A.I.A.A. J.*, 41:1–10, 1971.
- García M. Turbidity currents. In L. Brekhovskikh, K. Turekian, K. Emery, and C. Tseng, editors, *Encyclopedia of Earth System Science*, volume 4, pages 399–408. Academic Press, Inc., New York, 1992.
- Hallworth M., Huppert H., and Ungarish M. Axisymmetric gravity currents in a rotating system: experimental and numerical investigations. *Journal of Fluid Mechanics*, 447:1–29, 2001.
- Hoult D. Oil spreading in the sea. *Ann. Rev. Fluid Mechanics*, 4:341–368, 1972.
- Huppert H. and Simpson J. The slumping of gravity currents. *Journal of Fluid Mechanics*, 99:785–799, 1980.
- Marino B., Thomas L., and Linden P. The front condition for gravity currents. *Journal of Fluid Mechanics*, 536:49–78, 2005.
- Shin J., Dalziel S., and Linden P. Gravity currents produced by lock exchange. *Journal of Fluid Mechanics*, 521:1–34, 2004.
- Zhou J. R.A.S.B. and Kendall T. Mechanics for generating coherent packets of hairpin vortices. *J. Fluid Mech.*, 387:353–396, 2005.